

Poly(lactic acid)/poly(butylene succinate) dual-layer membranes with cellulose nanowhisker for heavy metal ion separation

Lau Kia Kian^a, Mohammad Jawaid^{a,*}, Mohamed Mahmoud Nasef^b, Hassan Fouad^c,
Zohab Karim^{d,e}

^a Laboratory of Biocomposite Technology, Institute of Tropical Forestry and Forest Products (INTROP), Universiti Putra Malaysia, 43400 Serdang, Selangor, Malaysia

^b Advanced Materials Research Group, Center of Hydrogen Energy, Malaysia-Japan International Institute of Technology (MJIIIT), Universiti Teknologi Malaysia, Jalan Sultan Yahya Petra, 54100 Kuala Lumpur, Malaysia

^c Department of Applied Medical Science, Community College, King Saud University, PO Box 10219, Riyadh 11433, Saudi Arabia

^d MoRe Research Örnköldsvik AB, SE-891 22 Örnköldsvik, Sweden

^e Institute of Architecture and Civil Engineering, South Ural State University, Chelyabinsk 454080, Russia

ARTICLE INFO

Keywords:

Poly(lactic acid)
Poly(butylene succinate)
Cellulose nanowhisker
Dual-layer membranes

ABSTRACT

In this study, poly(lactic acid) (PLA)/poly(butylene succinate) (PBS) dual-layer membranes filled with 0–3 wt% cellulose nanowhisker (CNWs) were fabricated with aim to remove metal ions from wastewater. An integrated method was employed in the membrane fabrication process by combining water vapor-induced and crystallization-induced phase inversions. The membrane thickness was measured in between 11 and 13 μm , which did not pose significant flux deviation during filtration process. The 3% CNW filled membrane showed prominent and well-laminated two layers structure. Meanwhile, the increase in CNWs from 0 to 3% loadings could improve the membrane porosity (43–74%) but reducing pore size (2.45–0.54 μm). The heat resistance of neat membrane enhanced by 1% CNW but decreased with loadings of 2–3% CNWs due to flaming behavior of sulphated nanocellulose. Membrane with 3% CNW displayed the tensile strength (23.5 MPa), elongation at break (7.1%), and Young's modulus (0.75 GPa) as compared to other samples. For wastewater filtration performance, the continuous operation test showed that 3% CNW filled membrane exhibited the highest removal efficiency for both cobalt and nickel metal ions reaching to 83% and 84%, respectively. We concluded that CNWs filled dual-layer membranes have potential for future development in the removal of heavy metal ions from wastewater streams.

1. Introduction

Membrane technology has been greatly grown for separation and purification applications in various fields including wastewater treatment, haemodialysis, food and beverages and pharmaceutical in past few decades. Particularly, membrane filtration techniques have been widely used in separating various organic and chemical pollutants [1]. In recent decades, the growing use of chemicals in various industries such as tanneries, textiles, electronic, automobile and mining resulting in water contamination with heavy metal ions posing serious health issues (human, animal and aquatic life) because of their acute toxicities and carcinogenic nature [2]. Thus, separation of such heavy metal ions has been one of major separation tasks of various technologies including membrane separation technology [3]. Moreover, the employment of

membrane technology for wastewater filtration is also regarded as reliable and effective approach to mitigate the crisis of water scarcity [1].

Polymeric materials are widely used in producing membrane owing to their simple processability and fulfilled characteristics for water filtration. Meanwhile, it has also been receiving the interest from scientists and researchers to work on the fabrication techniques to produce high performance membrane [4]. Reportedly, polymeric membranes are fabricated by phase inversion [5,6], electro-spinning [7], freeze-drying [8], and particulate leaching/solvent merging [9,10] techniques. Phase inversion is commonly known as a method for fabricating porous membrane network because of its ability to form a polymer skeleton, in which hierarchically linked to the pores organized from micro to nanoscale. The fabrication process is induced by the non-solvent,

* Corresponding author at: Biocomposite Technology Laboratory, INTROP, Universiti Putra Malaysia, 43400 Serdang, Selangor, Malaysia.
E-mail address: jawaid@upm.edu.my (M. Jawaid).

<https://doi.org/10.1016/j.ijbiomac.2021.10.042>

Received 5 July 2021; Received in revised form 4 October 2021; Accepted 6 October 2021

Available online 13 October 2021

0141-8130/© 2021 Elsevier B.V. All rights reserved.

especially like water, which normally utilized in the exchange with solvents for precipitating polymeric components [11,12].

Amongst polymer components, poly(lactic acid) (PLA) is advantageous for membrane fabrication due to its stable crystallization and porous network formation, good thermal tolerance, great mechanical as well as its sustainable and renewable natures [13]. Tanaka et al. [6] had prepared porous poly(L-lactic acid) membranes for microfiltration application by using water induced phase inversion technique. Lately, Minbu et al. [5] fabricated poly(L-lactic acid) microfiltration membranes using water induced phase inversion with the aid of surfactant, and more recently Chinyerenwa et al. [14] utilized hot water droplets induced phase inversion to produce porous polylactic acid (PLA) membranes. Besides this, Gao et al. [15] had studied the pore formation of poly(L-lactic acid) by applying controlled polyethylene oxide additives, and also Phaechamud and Chitrattha [16] investigated the porous formation of poly(DL-lactic acid) by using various co-solvents.

Recently, nano-sized fillers like nanocellulose [17,18], zeolites [19,20], and carbon nanotubes [21,22] have been incorporated into the polymeric membrane structure in order to improve the porosity, thermal properties, mechanical strength, flux permeability, anti-fouling and separation enhance capability [23]. Nanocellulose, is a cellulose derivative product obtained from natural fibers. It is a promising nano-filler for reinforcing polymeric component by attributing to its heat tolerance, high stiffness and inherent nature of environmental friendly characteristics [24–26]. Also, the large number of reactive functional groups attached on the nanocellulose surface can contribute to the great interaction with polymeric components [27,28]. Zhong et al. [18] had reported the fabrication of polysulfone/sulfonated polysulfone composite membrane by improving its hydrophilicity and mechanical properties using cellulose nanofibers. Furthermore, nanocrystalline cellulose was incorporated in polysulfone composite by Bai et al. [17] to produce porous membrane in good connectivity and enhanced mechanical strength. In accordance with literature studies, nanocellulose particles could form percolating networks by agglomeration, which eventually influenced the polymer interfaces and induced large void formation within membrane [29,30].

Dual-layer membrane is a bilayer porous structure comprising of two different polymeric components with distinct properties. Configuration of dual-layer membrane had been regarded as a well-controlled feature to effectively interact with dispersed nanoparticles in both of the top and bottom polymeric layers. The interaction was generally attributing to the localising effect by the preserved intrinsic characteristic in each separated polymer layer [1]. Meanwhile, the introducing nanoparticles in dual-layer membrane could improve its separation performance in terms of surface hydrophilicity, flux permeability and anti-fouling properties. Li et al. [31] fabricated a PES/P84 dual-layer membrane with zeolite beta particle added to PES upper layer to enhance permeability and selectivity for O₂/N₂ and CO₂/CH₄ gas separation. Bonyadi et al. [32] incorporated clay particles in both of the outer and inner layers of a PVDF/PVDF dual-layer membrane to improve the mechanical strength and modified the surface tension of polymer layers for direct contact membrane distillation process. Currently, Zuo et al. [33] added Al₂O₃ nanoparticles into the inner layer of PVDF/Ultem dual-layer hollow fiber membranes to improve flux performance and mechanical strength for vacuum membrane distillation. Liu et al. [34] also reported that the reduced pore size and the improved hydrophilicity of CA/PVDF dual-layer membrane was obtained by the increased TiO₂ nanoparticle loading in the outer layer. Therefore, desirable dual-layer membrane characteristics could be modified through the incorporation of nanoparticles. However, the dual-layer membranes incorporating organic nanofillers such as nanocrystalline cellulose have not been reported in literature.

Considering membrane preparation methods, water vapor-induced phase inversion is considerably facile technique to produce porous membranes that involves coagulation of a polymer solution in a vapourized water, and ultimately leads to the polymer precipitation.

However, the uncontrolled exchange rate of the water vapor and solvent phases tends to induce a delamination in the dual-layer polymer matrix, which potentially causing a degradation in the membrane properties [1,35]. To overcome this problem, an integrated method combining water vapor-induced and crystallization-induced phase inversions is applied in this study to fabricate a new dual-layer membrane composed of poly(lactic acid) (PLA) and poly(butylene succinate) (PBS) with cellulose nanowhisker (CNWs) as functional filler. The CNWs not only plays a significant role in regulating the polymer phases separation and crystallization but also triggers hydrophilicity nucleation effect beside serving as a pore-forming agent. This fabrication concept is motivated by the absence of any investigation on the utilisation of CNWs as fillers to generate PLA/PBS dual-layer polymeric membrane with high performance in separation metal ions. Meanwhile, the fabricated dual-layer membranes undergo various evaluations of their chemical, physical, thermal, and mechanical properties with respect to the variation of nanocellulose fillers content. Also, the wastewater filtration performance of the dual-layer membranes was evaluated for separation of heavy metals such as Co²⁺ and Ni²⁺ ions from solutions.

2. Experimental

2.1. Materials and chemicals

Poly(lactic acid) (PLA) pellet (average MW of 75 kg/mol, density of 1.24 g/cm³ and polydispersity of 1.6) and poly(butylene succinate) (PBS) pellet (average MW of 12 kg/mol and density of 1.26 g/cm³), were purchased from PTT Public Co. Ltd. (Bangkok, Thailand). *N,N*-dimethylformamide (DMF) (≥ 99.8% purity), chloroform (CHCl₃) (≥ 99.5% purity), cobalt (II) chloride hexahydrate (CoCl₂·6H₂O) (≥ 98% trace metal basis), nickel (II) chloride hexahydrate (NiCl₂·6H₂O) (≥ 98% trace metal basis), sulfuric acid (H₂SO₄) (95–98%) and dialysis tube (10 mm average flat width, 2000 MWCO) were purchased from R&M Chemicals. All chemicals were research grade and used as received.

2.2. Preparation of cellulose nanowhisker (CNW)

Roselle MCC was utilized as starting material for CNW preparation as reported in our previous work [36]. Hydrolysis at temperature of 45 °C was conducted to a 2.5 g MCC with 80 mL of (50% w/w) sulfuric acid solution under vigorous mechanical stirring. At the end of acid hydrolysis, the resultant white colloidal suspension was mixed with cold water and centrifuged at 6000 rpm until a pH value close to 3 was reached. Subsequently, the collected white cloudy suspension was subjected to ultrasonication for 15 min with amplitude of 40% at constant 20 kHz frequency and 500 W power output. The suspension was thereafter left for 1 h to sediment the undesired macro-size cellulosic component. Afterwards, the suspension was dialyzed with distilled water to reach value of pH 5. Lastly, the supernatant nanocellulose suspension was collected and freeze-dried.

2.3. Preparation of dual-layer membranes

A 10 wt% PLA and 5 wt% PBS solutions were prepared separately by mixing in DMF solvent (on the basis of 100 wt%) at 60 °C until fully dissolved. Initially, the PLA polymer solution was casted on a petri dish as bottom dope layer and then partially solidified by cooling at room temperature for 5 min, followed by casting the second dope solution containing PBS as a top layer on the same petri dish. The petri dish was subsequently placed in a heated bath container filled with water vapor for 5 min to induce the phase inversion for precipitation process as shown in the schematic diagram. A schematic diagram of experimental phase inversion process for dual layer membrane precipitation is presented in Fig. 1. Thereafter, the precipitate-containing solution was subjected to freezing in refrigerator and then gently washed with chloroform to remove the DMF solvent. At the end, a pure PLA/PBS

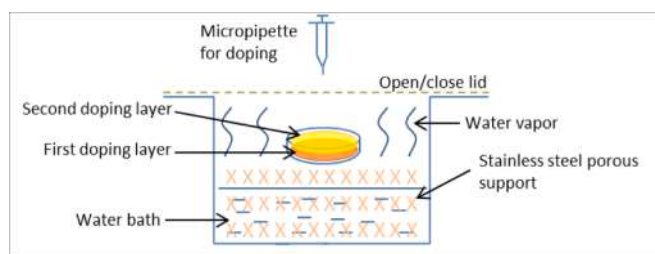


Fig. 1. Schematic diagram of experimental phase inversion process for dual layer membrane precipitation.

dual-layer membrane was obtained after drying in vacuum oven to remove remained water and solvent traces. For nanocellulose reinforced membranes, a different amount of nanocellulose were loaded in range of 1–3 wt% during the first mixing step with DMF solvent at 60 °C under vigorous stirring. A series of subsequent treatment processes similar to the fabrication of pure PLA/PBS dual-layer membrane were then carried out. The denotations of obtained dual-layer membranes for pure PLA/PBS and nanocellulose filled PLA/PBS with their formulation with different loadings are summarized in Table 1.

2.4. Nanocellulose characterization

The structural morphology of CNW particles was observed with JEOL JEM-2100F transmission electron microscope (TEM). Preparation of specimens was conducted by negatively staining the CNWs with 2 wt% uranyl acetate solution prior to deposition on copper grid substrate for drying. Subsequently, the CNW samples undergo observation with TEM operating at 200 kV accelerating voltage and the obtained data was processed using Image J software. Furthermore, the Brunauer–Emmett–Teller (BET) analysis was used to determine the specific surface area of CNWs using a Micromeritics ASAP 2000 instrument, and the samples were degassed by flowing of nitrogen gas at 60 °C for 30 min before analysis.

2.5. PLA/PBS dual-layer membranes characterization

The top surface, bottom surface, and cross section morphology of dual-layer membranes were investigated by a field emission electron microscope (FESEM) under an accelerating voltage in the range of 10–20 kV. Before FESEM observation, the membranes were coated with platinum *via* sputtering to avoid charging effect. For cross-sectional analysis, the membranes were fractured after dipping in liquid nitrogen prior to gold coating and mounting on sample holders. In addition, the thickness of produced dual-layer membranes was measured with a YASUDA digital film thickness gauge. BET analysis was employed to determine the membrane porosity and average pore size using a Micromeritics ASAP 2000 instrument after degassing in the flow of nitrogen gas at 60 °C for 30 min prior to analysis. The compositional structure of the membrane samples was examined with Perkin Elmer 1600 Infrared spectrometer (FTIR) within 500–4000 cm^{-1} wavenumber range. The changes in the crystallinity of the membranes samples was

Table 1

Denotations of fabricated PLA/PBS dual-layer membranes and their formulation with different nanocellulose loadings.

Denotations of dual-layer membrane samples	Formulation (on the basis of 100 wt% DMF)		
	PLA (wt %)	PBS (wt %)	Nanocellulose (wt %)
C-neat	10	5	0
C-I	10	5	1
C-II	10	5	2
C-III	10	5	3

monitored with a SHIMADZU XRD-6000 X-ray diffractometer (XRD) with scanning speed from 5° to 60° at 2 °C/min stepwise and a TA Instruments Q20 differential scanning calorimeter (DSC) with a temperature scanning range from 25 °C to 200 °C at 5 °C/min heating rate under nitrogen atmosphere. The collected data from DSC was used to calculate the crystallinity degree of PLA and PBS as below Eq. (1) and Eq. (2), respectively.

$$X_c \text{ of PLA} = \frac{\Delta H_m}{93.6} \times 100\% \quad (1)$$

$$X_c \text{ of PBS} = \frac{\Delta H_m}{100.7} \times 100\% \quad (2)$$

where, ΔH_m is the melting enthalpy of respective polymer.

Apart from that, the thermal stability of the samples was investigated with TA Instruments Q500 thermogravimetric analyzer (TGA) in a temperature range of 25–1000 °C at 20 °C/min heating rate. An Instron 4400 Universal Tester was used to study the mechanical properties with respect to tensile strength and elongation at break of the samples according to the ASTM D882–12 under a fixed 12.5 mm/min crosshead speed. Also, the wettability of the membrane surface was studied with a KRUSS DSA-100 goniometer and the contact angle was determined after a 2.5 μL water dropping for 2 s.

2.6. Performance of dual-layer membranes

To evaluate the wastewater filtration performance, model solutions of Co^{2+} and Ni^{2+} were used. Particularly, 50 mg/L solutions containing Co^{2+} and Ni^{2+} were prepared separately and used as a stock for all batch and continuous adsorption experiments through a 0.4 g/L solid membrane. In batch adsorption mode, each membrane was incubated in a 100 mL volume of metal ion solution for 180 min. Meanwhile, the removal efficiency (R_e) for metal ions was calculated with the following Eq. (3).

$$R_e (\%) = 1 - \frac{C_p}{C_f} \times 100 \quad (3)$$

where, C_p and C_f are the metal ion concentrations of permeate and feed solutions respectively, which determined with inductively coupled plasma optical emission spectrometry (ICP-OES). Also, the adsorbed capacity (Q_e) for metal ions was calculated using the Eq. (4).

$$Q_e (\text{mg/g}) = \frac{(R_e \times C_f)}{m} \quad (4)$$

where, m is the effective mass of membrane subjected to adsorption in metal ion solutions.

For continuous adsorption mode, a 100 mL volume of metal ion solution was allowed to flow through a dead-end filtration cell for 180 min under 0.1 MPa applied pressure with a membrane having an effective area of 16 cm^2 . Similarly, the removal efficiency and adsorbed capacity of metal ions were determined using the Eq. (3) and Eq. (4), respectively. Additionally, the flux of pure water and metal ion solution (J) was measured at each 30 min time interval following the Eq. (5).

$$J = \frac{V}{A \times t} \quad (5)$$

where, V is the volume of pure water or metal ion solution (L), A is the effective area of membrane (m^2), and t is the filtration time. Anti-fouling testing was also carried out on the best optimized membrane by second filtration cycle to determine the reversible fouling (R_r), irreversible fouling (R_{ir}), total fouling ratio (R_t), flux recovery of pure water (FR_w) and metal ion solution (FR_p), using Eq. (6), Eq. (7), Eq. (8), Eq. (9), and Eq. (10), respectively.

$$R_r = \frac{J_{w2} - J_{p1}}{J_{w1}} \times 100\% \quad (6)$$

$$R_{ir} = \frac{J_{w1} - J_{w2}}{J_{w1}} \times 100\% \quad (7)$$

$$R_t = 1 - \frac{J_{p1}}{J_{w1}} \times 100\% \quad (8)$$

$$FR_w = \frac{J_{w2}}{J_{w1}} \times 100\% \quad (9)$$

$$FR_p = \frac{J_{p2}}{J_{p1}} \times 100\% \quad (10)$$

where, J_{w1} is the pure water flux, J_{w2} is the water flux of cleaned membrane, J_{p1} is the metal ion solution flux, and J_{p2} is the metal ion solution flux of the cleaned membrane.

2.7. Statistical analysis

The BET, mechanical test, and water contact angle data (means, $M \pm$ standard deviation, SD) were obtained with replicates for each membrane sample to provide reproducibility proof in each characterization section of morphology, mechanical and filtration performance, respectively. Statistical comparisons were analysed by using ANOVA (t -test) and the differences with $p \leq 0.05$ (95% confidence level) were considered statistically significant.

3. Results and discussion

3.1. Morphology of nanocellulose and PLA/PBS dual-layer membranes

The CNWs was proved to have a rod-like shape as illustrated TEM image (Fig. 2). The measured average size for the CNW rods was in 119.4 ± 0.2 nm length, 18.1 ± 0.5 nm diameter and with aspect ratio of 6.6 ± 0.4 . Meanwhile, specific surface area by BET analysis was 19.32 ± 0.04 m²/g. The isolated CNWs morphology has been reported in our previous published article [36], and it is in the agreement of isolated CNWs. Furthermore, detailed morphology using TEM, SEM and Atomic Force Microscopy (AFM) is also mentioned in our previous article [36].

Fig. 3 shows the FESEM images of C-neat, C-I, C-II and C-III membranes. All membrane samples revealed dense top surface (Fig. 3a-d) and porous bottom surface (Fig. 3i-l), which rendered by water vapor-induced phase inversion fabrication [35]. The propagating circular lines could be observed on the top surfaces for C-I (Fig. 3b), C-II (Fig. 3c) and C-III (Fig. 3d) membranes when compared to the apparently order less surface of C-neat membrane (Fig. 3a). This implies that the PBS polymer chains were greatly sealed in the membranes by the incorporation of CNWs [37]. Under magnified viewing, the surface

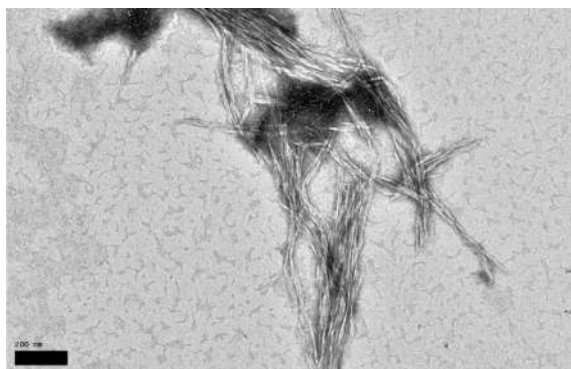


Fig. 2. TEM image of formed CNW.

morphology was found to be smoother for C-I (Fig. 3f) as compared with C-neat membrane (Fig. 3e), confirming the improved interaction between polymer chains after the addition of CNWs. With the increased CNWs loadings beyond 1 wt%, rougher surfaces were observed for C-II (Fig. 3g) and C-III (Fig. 3h) membranes. This trend was attributed to the induced steric hindrance caused by the considerable amount of CNW that resulted in the formation of bulky polymer chains [38,39]. Furthermore, it has also been shown that better morphology was observed when the low conc. of CNWs was loaded during fabrication of composite membranes. Each nanocomposite membrane exhibited well-distributed CNWs on their top surface, and this could endow them with a good initial contacting surface area for adsorbing heavy metal ions in wastewater treatment [2,27]. As viewed from bottom-surface images, C-neat (Fig. 3i) presented apparently tough structure with dented surface. A tremendously change of dented features were observed for C-I (Fig. 3j) and C-II (Fig. 3k) membranes, owing to the unstable exchange rate that occurred between DMF and water vapor for polymer crystallization [16,40,41]. Furthermore, the incorporation of CNWs contributed to the formation of small cell-like pore for C-I, C-II and C-III membranes (Fig. 3n-p), as compared to the C-neat membrane (Fig. 3m), which displaced little porous feature, and this is because the CNW particles acted as a nucleating agent for promoting cell-sized porous surface. During the crystallization process, small crystals domains were initially formed, and these small crystals subsequently cultivated into bigger crystals to induce pore formation because of coalescence occurred in the later stage [42,43].

Likewise, the membrane thickness determined in this work was found in the range of 11 to 13 μ m, which did not pose significant flux deviation. From Table 2 depicting BET data, the porosity was gradually improved from $43 \pm 0.036\%$ for C-neat to $67 \pm 0.024\%$ for C-I membrane, and then further increased to $71 \pm 0.053\%$ and $74 \pm 0.028\%$ for C-II and C-III membranes, respectively. Meanwhile, the average pore-size was found decreasing from C-neat (2.45 ± 0.019 μ m) membrane to C-I (1.13 ± 0.017 μ m), C-II (0.86 ± 0.024 μ m), and C-III (0.54 ± 0.015 μ m) following the addition of CNWs (Table 2), the increase of CNWs amount, which triggered the generation of larger number of small growing crystals domains could be the reason for decrease in pore-size distribution. Herein, higher porosity was obtained, owing to the greater coalescence effect between the grown crystals. However, due to the saturation state achieved between the CNWs and polymers, the growth of small crystals was suppressed and hence a reduction in the pore size took place with the increase in CNW loadings in the membranes [43,44]. In cross-sectional viewing for C-neat membrane (Fig. 3q) confirm the mixing of PLA polymer layer with PBS polymer layer. Meanwhile, the PBS layer was observed extending downwards to the PLA layer, implying the presence of good interfacial adhesion between these two polymers [34]. Instead, the C-I membrane (Fig. 3r) showed leaf-like porous structure, but the distinctly two layers were not likely observed in the membrane. This was attributed to the simultaneously increasing free volume in both PLA and PBS polymers by mixing with 1 wt% CNWs, which greatly enhanced both polymers miscibility [45,46]. When 2 wt% CNW filler was introduced, the finger-like pore feature began to emerge in C-II membrane (Fig. 3s), and this feature transition implies that an enhancement in polymer rigidity occurred. For C-III (Fig. 3t), a prominent finger shaped porous structure was observed when 3 wt% CNW fillers were incorporated into the membrane, signifying the presence of stable crystallized dual-layer polymer structure [34,47]. The C-III membrane revealed much significant layers of both PLA and PBS than that of C-II. Moreover, the PLA layer formed an interlocking structure with PBS layer for the C-III membrane via the hydrogen bonding generated by the adjacent hydroxyl groups in each polymer layer [35,45]. Thus, the lamination between the two layers was stronger in C-III compared to the C-neat membrane and other CNWs reinforced membranes.

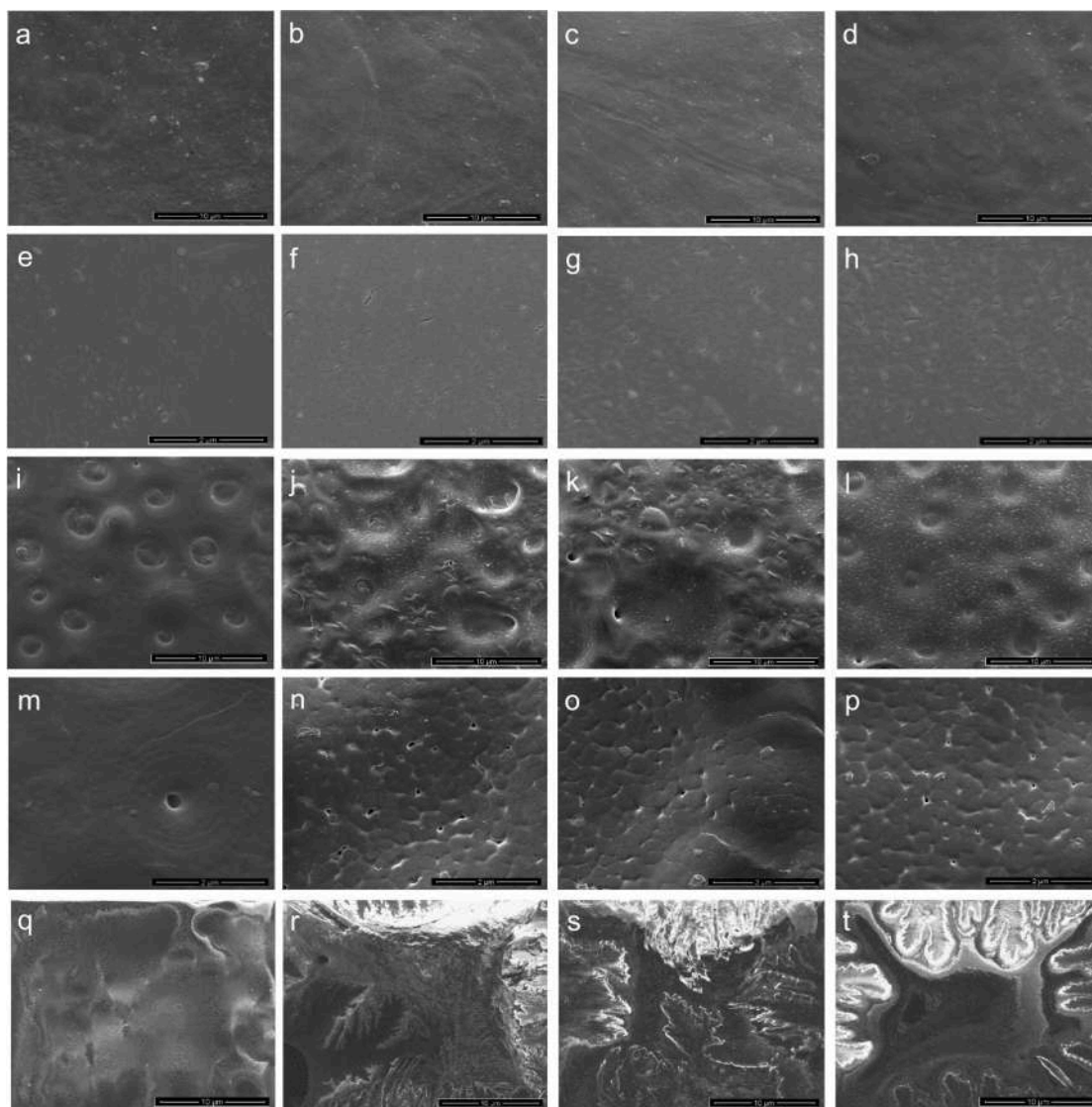


Fig. 3. FESEM images of C-neat (a, e, i, m, q), C-I (b, f, j, n, r), C-II (c, g, k, o, s), and C-III (d, h, l, p, t) membranes for top-surface at 10000 \times (a-d) and 50,000 \times (e-h) magnifications; bottom-surface at 10000 \times (i-l) and 50,000 \times (m-p) magnifications; cross-sectional view at 10000 \times (q-t) magnification morphology.

Table 2

BET data for porosity and average pore size of membranes.

Membranes	Porosity (%)	Average pore size (μm)
C-neat	43 \pm 0.04 ^a	2.45 \pm 0.02 ^a
C-I	67 \pm 0.02 ^b	1.13 \pm 0.02 ^b
C-II	71 \pm 0.05 ^c	0.86 \pm 0.02 ^c
C-III	74 \pm 0.03 ^d	0.54 \pm 0.01 ^d

^{a-d}Values within the same column with various superscripts indicate significant differences ($p \leq 0.05$).

3.2. Physicochemical property

The changes in chemical structure were monitored with FTIR (Fig. 4a). From Fig. 4a, the nanocellulose filled membranes showed closely similar FTIR spectra with C-neat membrane in the region of 500–2000 cm^{-1} . For instance, significant absorbance peaks were observed for each membrane sample at 1088 cm^{-1} (C-OH bending), 1153 cm^{-1} (C-O-C stretching), 1448 cm^{-1} (CH_3 stretching) and 1712 cm^{-1} (C=O vibration), which signifies the typical characteristics of the membrane's polymer molecules [37,48]. Noticeably, the peak at around

3410 cm^{-1} absorbance became sharper after the addition of nanocellulose and this resembles the cellulose hydroxyl groups (O–H vibrational stretching) indicating the achievement of good physically mixing of nanocellulose within polymeric components [27,49]. Moreover, the absence of new absorbance peak from the FTIR spectra had proved that no chemical reaction occurred in all nanocellulose filled membranes.

XRD diffractograms of the membranes is presented in Fig. 4b. According to literature, the PLA has main diffraction peaks at $2\theta = 16.7^\circ$ (200), 19.2° (203), and 22.3° (110) representing α -form of PDLA or PLLA crystals with pseudo-orthorhombic system, whereas, PBS showed main diffraction peaks at about $2\theta = 19.6^\circ$ (002), 21.8° (012), and 22.7° (110) resembling α -form with monoclinic system [49,50]. According to Fig. 4b, predominant peaks at around 16.8° , 20.4° , and 22.5° can be clearly seen in all membrane samples. Meanwhile, a broad peak was observed for each sample extending from 19° to 26° that comprised the 20.4° sharp peak and a 22.5° shoulder peak. These results might be contributed by the overlapping of the crystalline peaks of both PLA and PBS components in the membrane where the adhered interactions between the two polymeric layers were conceived [50]. However, the presence of broadly vast peaks might cover the undetermined regions in

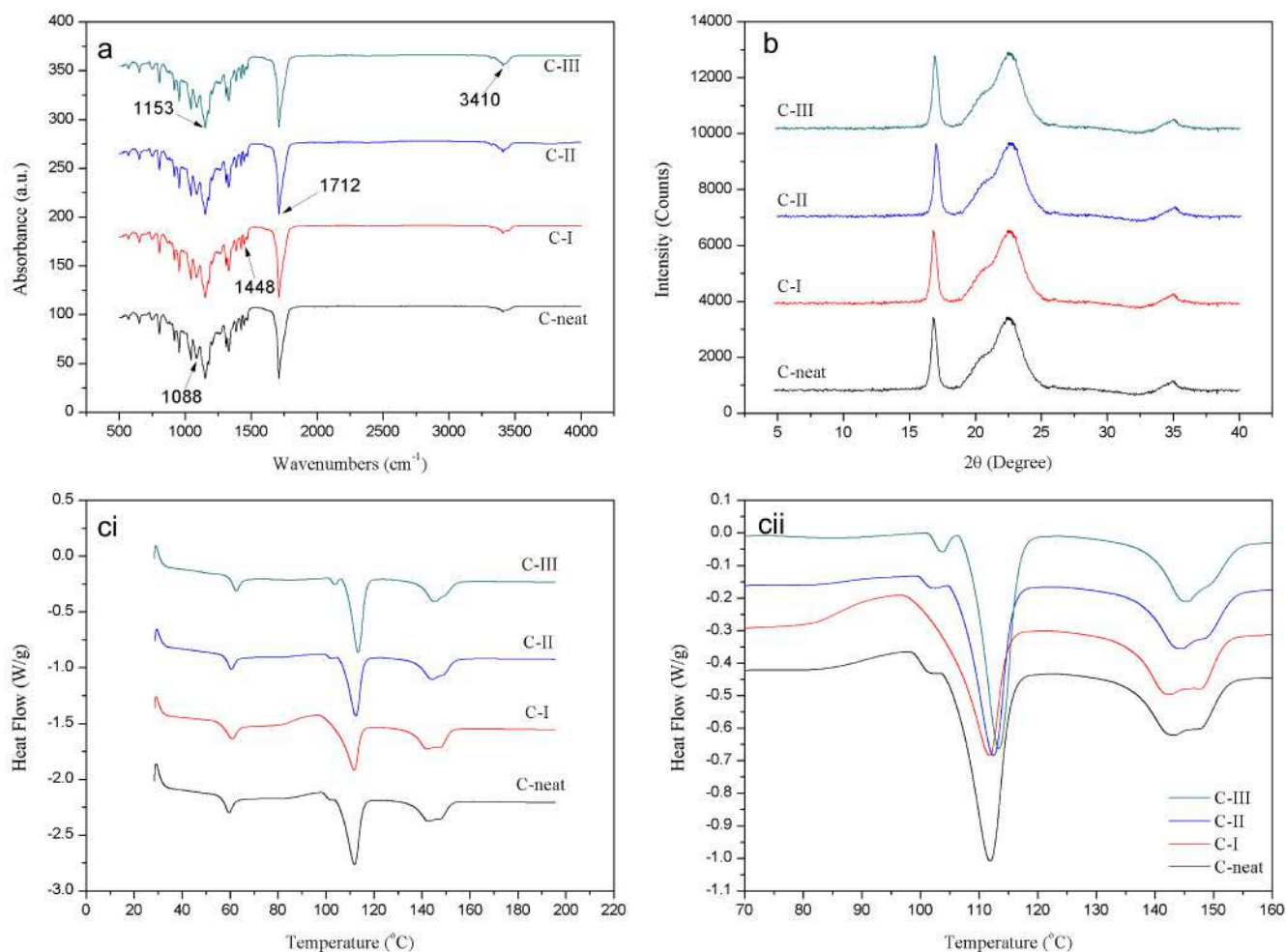


Fig. 4. Various changes in properties of dual-layer membranes observed in: (a) FTIR spectra (b) XRD diffractograms and (ci and cii) full and zoomed DSC curves, respectively.

this XRD diffractogram representing the level of the adherence between the two polymeric layers is invalid. Moreover, distinct peak at 16.8° originated from PLA polymer having similar intensity in all membranes. This showcased the well-define crystalline characteristics for the PLA component existing in all the dual-layer membrane samples [49,51]. A slight peak left shifting could be observed for C-I with 16.7° peak as compared to C-neat with 16.8° peak, revealing the unordered crystal arrangement in the C-I membrane. Nonetheless, the C-II and C-III exhibited their peaks with 17.0° and 17.1° respectively in right shifting to the C-neat, which correlated with the improved crystal lattice organizations [14,47].

DSC curves of the fabricated membrane samples and their

corresponding thermal properties data obtained only from first heating runs are presented in Fig. 4c and Table 3, respectively. The glass transition temperature (T_g) of PLA was mildly enhanced for C-I, C-II and C-III membranes when compared to the C-neat, signalling the integration of nanocellulose in PLA could reduce its polymeric chain mobility (Fig. 4ci) [52]. Beyond 80°C temperature (Fig. 4cii), the C-neat membrane revealed its exothermic peak at 98.1°C (T_c of PLA) accompanied by a second small exothermic peak at 101.7°C (T_c of PBS). Interestingly, the small secondary exotherm, was not observed in C-I membrane, which rather had been overlapped by the broadly large exothermic peak at 111.9°C . This was likely showing that the distinct crystallization behavior of both PLA and PBS polymers had somehow collapsed upon

Table 3

DSC analysis data of membrane samples.

Membranes	PLA					PBS			
	T_g ($^\circ\text{C}$) ^a	T_c ($^\circ\text{C}$) ^b	T_m ($^\circ\text{C}$) ^c	ΔH_m (J/g) ^d	X_c (%) ^e	T_c ($^\circ\text{C}$) ^b	T_m ($^\circ\text{C}$) ^c	ΔH_m (J/g) ^d	X_c (%) ^e
C-neat	60.1	98.1	143.2	32.7	34.9	101.7	112.0	17.1	17.0
C-I	60.9	96.9	142.6	33.8	36.1	–	111.9	19.0	18.9
C-II	60.7	99.4	144.5	34.1	36.4	104.6	112.5	20.3	20.2
C-III	62.6	101.3	145.4	35.2	37.6	106.2	113.4	21.4	21.3

^a Glass transition temperature.

^b Crystallization temperature.

^c Melting temperature.

^d Melting enthalpy.

^e Degree of crystallinity.

loading 1 wt% nanocellulose and subsequently contributed to the C–I membrane with assimilated structure [33,53]. Furthermore, the second observed exotherms in C-II and C-III implied the reformation of dual polymeric membrane structures, which were in line with the discussion in morphological FESEM section. It could be ascribed to the faster growth of PLA and PBS crystals that were promoted by the great nucleating effect of nanoparticles at the 2 and 3 wt% nanocellulose loadings [39,49].

Furthermore, the PLA and PBS melting temperatures (T_m) (Table 3) were slightly decreased for C–I membrane compared to C-neat, possibly owing to the immiscibility between polymers and nanocellulose to some extents. Meanwhile, the melting temperatures had increased for C-II and C-III membranes. This was attributed to the great localization effect of CNWs in the dual-layer structure of the membrane leading to the better nanocellulose dispersion and adhesion in each polymer layer [54,55]. In addition, both melting peaks became sharper and narrower from C–I to C-III membranes, showing that the increase in filling of nanocellulose could improve the polymer integrity [41]. The melting enthalpy (ΔH_m) for both PLA and PBS components was recorded the highest value for C-III membrane. This trend might be imparted by the strong interfaces between CNWs and polymers as well as the strong adherence between the two polymeric layers *via* hydrogen bonding interaction [14,28]. Also, the estimated degrees of crystallinity (X_c) for both PLA and PBS polymers was increased from C-neat to C-III membranes (Table 3). Therefore, this confirms that the increment of nanocellulose loadings enhance the crystallinity of the dual-layer polymeric membrane structure and improve the components adherence and interfacial resistance.

3.3. Thermal stability, mechanical strength, and surface wettability analysis

Thermogravimetric and tensile analyses were employed to investigate the applicability of fabricated membranes in harsh conditions. From TGA curve in Fig. 5a, each membrane lost their initial weight in 50–160 °C temperature range due to the dehydration of absorbed water moisture from hydrophilic CNWs [16,52]. Beyond 200 °C temperature, those nano-filled membranes presented higher onset degradation temperature (T_{onset}) compared to the C-neat membrane. This indicates that the incorporation of CNWs tends to promote the thermal resistant of both polymer components *via* the hydroxyl groups interaction [46,56]. Regarding to the CNWs loadings effect, the onset degradation temperatures were slightly decreased from C–I to C-II membranes, whereas, gradually reduced for the membranes from C-II to C-III (Table 4), thus,

Table 4

TGA analysis data of membrane samples.

Membranes	T_{onset} (°C) ^a	T_{peak} (°C) ^b	W_{loss} (%) ^c	$W_{residue}$ (%) ^d
C-neat	315.8	354.6	89.4	5.4
C-I	326.8	355.8	89.1	5.6
C-II	324.7	355.3	88.5	6.1
C-III	317.2	355.0	87.9	6.4

^a Onset degradation temperature.

^b Degradation peak temperature.

^c Weight loss.

^d Char residual weight.

the onset thermal degradation temperature of membranes was in the order of C-I > C-II > C-III and the loading of CNWs was in opposite order, thus, we believe that high amount of CNWs in the membranes and low degradation temperature of CNWs responsible for low thermal profile of composite membranes. Furthermore, the high density of ester sulfate groups presence in the CNWs (with respect to high amount of loaded CNWs) could also be another possible reason for low thermal degradation temperature of membranes as reported in our previous published article [36]. Furthermore, the sign of low residue formation ($W_{residue}$) in responding to the high weight loss (W_{loss}) was observed in all membrane samples (Table 4). The C-III membrane revealed significantly high weight residue owing to the flame retardant of crystalline nanocellulose [28,46]. Additionally, from DTG curve, the C–I membrane had the greatest thermal stability between those membranes with its degradation peak temperature (T_{peak}) at 355.8 °C.

For mechanical test (Fig. 5b), both tensile strength and elongation at break were improved for C-II and C-III membranes when compared with C-neat membrane. However, the C–I membrane presented lower elongation at break and tensile strength than the other membrane samples. This attributed to the distinct two polymeric layers structures in C-neat, C-II and C-III membranes imparting them with better stress transfer property [6,28]. As for C–I membrane, its collapsed layered structure resulted in the PBS upper layer unlikely to reduce stress-strain forces delivered to the PLA bottom layer. Additionally, the increment of nanocellulose from 2 to 3 wt% tremendously enhanced the elongation at break for C-III membrane besides the improvement of tensile strength. This was resulted from the combined effect of interactions within the CNWs and matrix and small average pore size in C-III membrane allowing great stress transfer between nanocellulose and polymers [15,33]. Also, the Young's modulus measured for membranes filled with CNWs was consistent with the improvement of the tensile strength

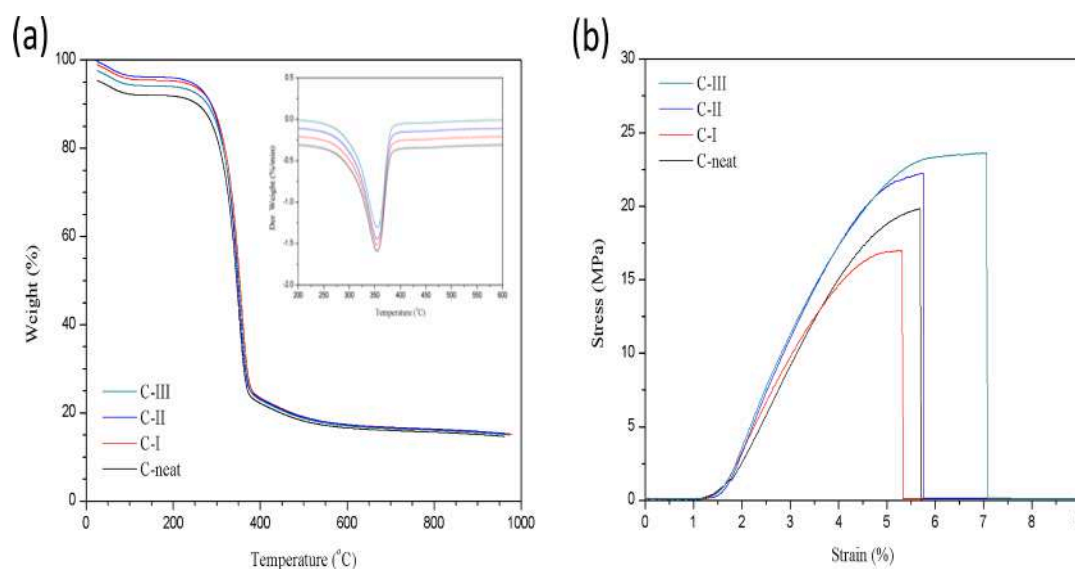


Fig. 5. (a) TGA curves (with plotted DTG curves) and (b) mechanical stress-strain curves of dual-layer membranes.

Table 5

Tensile properties data of membrane samples.

Membranes	Tensile strength (MPa)	Elongation at break (%)	Young's modulus (GPa)
C-neat	19.7 ± 0.15 ^a	5.7 ± 0.08 ^a	0.67 ± 0.05 ^a
C-I	16.9 ± 0.14 ^b	5.3 ± 0.06 ^b	0.66 ± 0.04 ^a
C-II	22.1 ± 0.15 ^c	5.8 ± 0.11 ^c	0.73 ± 0.06 ^b
C-III	23.5 ± 0.12 ^d	7.1 ± 0.09 ^d	0.75 ± 0.04 ^b

^{a-d}Values within the same column with various superscripts indicate significant differences ($p \leq 0.05$).

(Table 5). The C-III membrane gave the highest value of Young's modulus with 0.75 ± 0.04 GPa, whereas the C-I membrane displayed the lowest value of 0.66 ± 0.04 GPa. Hence, from mechanical test results, C-III membrane was regarded having the balanced elasticity, stiffness, and rigidity for withstanding water flux pressure in filtration process.

Apart from that, membranes surface wettability was evaluated by water contact angle as summarized in Table 6. A contact angle of ($69.2 \pm 0.08^\circ$ at top-surface and $70.4 \pm 0.05^\circ$ at bottom surface) was observed in C-neat membrane reflecting the PBS top and PLA bottom layers possessed relatively great water-favored characteristics probably promoted by their rough surface feature that formed during phase inversion process. Nonetheless, those nanocellulose filled membranes showed decreased contact angles, indicating the enhanced hydrophilicity on the membrane surfaces [41].

3.4. Membrane filtration performance

The Fig. 6 shows flux changes of pure water, Co^{2+} solution, Ni^{2+} solution for different dual-layer membranes. As can be seen, the flux of pure water, Co^{2+} and Ni^{2+} solutions were found to increase with the increase in nanocellulose loading and this is going along with the rise in hydrophilicity as indicated by the reduction in the contact angle with more filler in the membranes. It was because the higher nanocellulose amount could expose more polar hydroxyl groups (-OH) on the membrane surface, which thereby improved its reaction with water for high permeation [40,45]. Moreover, the constantly increasing flux for both pure water and metal ion solutions throughout those nanocellulose filled membranes might prove that the good migration and dispersibility of nanocellulose particles on each dual-layer membrane surface [2,34]. Theoretically, the decrease of average pore size from C-I ($1.13 \mu\text{m}$) to C-III ($0.54 \mu\text{m}$) membrane is supposed to reduce the permeability. However, the present membranes behaved conversely and the enhanced flux for the membranes in this work could be attributed to the compensation of improved porosity for the membrane from C-I (67%) to C-III (74%). In addition, hydrophilicity of composite membranes was also increased with loaded CNWs (Table 6), hence, porosity and surface hydrophilicity are dominating factors for high water flux of fabricated membranes with increase loading of CNWs [57,58].

The metal ions removal efficiency of the membranes was also examined by both batch and continuous modes of adsorptions and the obtained data are presented in Table 7. As can be observed, the C-II membrane showed highest removal efficiency for Co^{2+} ions standing at

Table 6

Water contact angle of dual-layer membranes with 0–3 wt% CNWs loadings.

Membranes	Water contact angle	
	Top surface ($^\circ$)	Bottom surface ($^\circ$)
C-neat	69.2 ± 0.08^a	70.4 ± 0.05^a
C-I	62.4 ± 0.05^b	67.0 ± 0.04^b
C-II	55.4 ± 0.07^c	62.1 ± 0.06^c
C-III	51.3 ± 0.09^d	59.7 ± 0.08^d

^{a-d}Values within the same column with various superscripts indicate significant differences ($p \leq 0.05$).

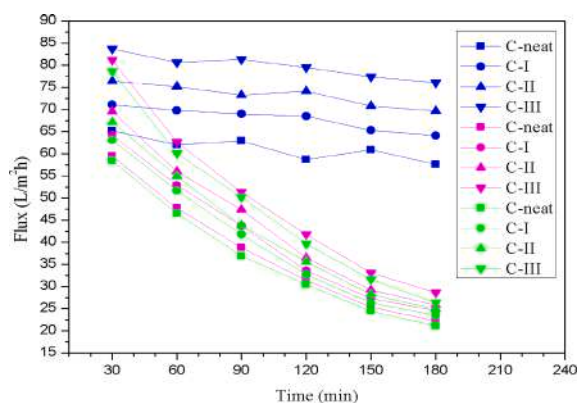


Fig. 6. Flux changes of pure water (blue line), Co^{2+} solution (purple line), Ni^{2+} solution (green line) for dual-layer membranes with 0–3 wt% CNWs loadings.

69% and 66% for Ni^{2+} ions in batch adsorption. On the other hand, the C-III showed the highest removal efficiency of 83% for Co^{2+} and 84% for Ni^{2+} ions under continuous adsorption mode. The low average pore size of C-III membrane most likely prevented the metal ions accessibility to the internal anchoring sites during the test under batch adsorption mode. However, the presence of the pressure applied in the continuous operation could aid in improving the adsorption of internal contact area for metal ions in C-III due to the increased solutions penetration through the membrane [59,60].

For C-I membrane, it exhibited remarkably lower metal ions removal in both operation modes compared to C-II membrane. It is due to the stronger size exclusion effect in C-I membrane from its less porosity network, which reduced the penetration of metal ions and ultimately facilitated metal ions attachment on nanocellulose hydroxyl function sites *via* ion-dipole interactions. This phenomenon was in agreement with the adsorption result obtained in studies reported in literature [2,58,61]. In this work, the continuous adsorption mode was more efficient in removing metal ions than the batch adsorption mode. The estimated adsorption capacity of C-III membrane in continuous mode was the highest with 103.8 mg/g for Co^{2+} and 105.0 mg/g for Ni^{2+} , while the lowest adsorption with 41.3 mg/g of Co^{2+} and 38.8 mg/g of Ni^{2+} ions for C-neat membrane (Table 7). The low adsorption capacity of C-neat membrane towards metal ions can be attributed to the intermolecular reaction with PLA polymer [2,62]. Thus, it was confirmed that C-III membrane possessed the highest metal ions adsorption capacity. Furthermore, for all composite membranes, higher adsorption capacity was recorded in cross-flow filtration mode rather than batch mode. During the batch mode the penetration capacity of metal ions is very low, thus, it is not possible for metal ions to capture the available functional groups present in the deep of membranes core. Consequently, in the cross-flow filtration mode, the applied pressure pushed the metal ions into the deep inside of membrane network. Therefore, the immobilization of metal ions with available deep functional groups increases the adsorption capacity of used membranes [62–66].

The obtained adsorption result was greater than the reported data by Liu et al. [62] using TEMPO-oxidized cellulose nanofibers for removing Cu^{2+} ions with approximately 32 mg/g adsorption capacity. Meanwhile, this work also gave better adsorption values than data reported in Danso et al. [63] in which 23.73 mg/g adsorption capacity of Zn^{2+} ions from metal coating wastewater and 10.50 mg/g adsorption capacity of Ba^{2+} ions from mining seep wastewater were observed using sulfur-ligand tethered cellulose nanofibers. Furthermore, the present results are comparable with those obtained by Liu et al. [60] who produced carboxylated cellulose nanocrystal/polyethyleneimine composite membrane for Cr^{3+} ion removal showing about 50 mg/g adsorption capacity, while Teow et al. [61] fabricated cellulose/gelatin composite hydrogel that showed 3 mg/g adsorption capacity of Cu^{2+} ions.

Table 7

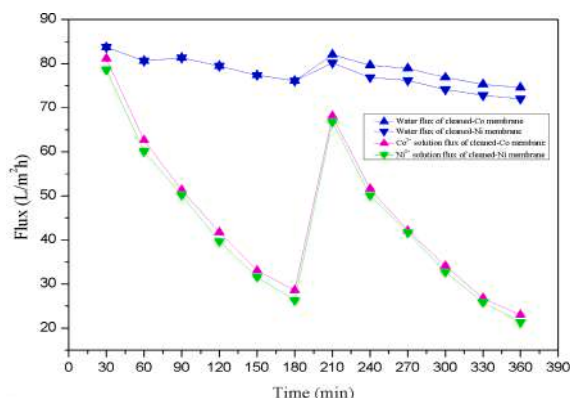
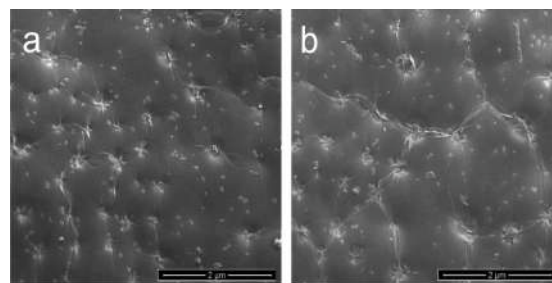
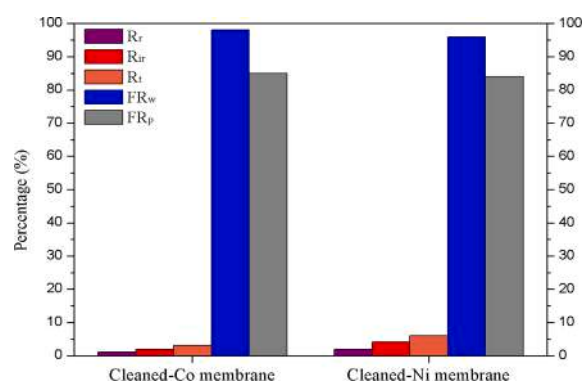
Metal ions adsorption capacity and removal efficiency by dual-layer membranes with 0–3 wt% CNWs loadings.

Membranes	Batch mode				Continuous mode			
	Adsorbed capacity (mg/g)		Removal efficiency (%)		Adsorbed capacity (mg/g)		Removal efficiency (%)	
	Co ²⁺	Ni ²⁺	Co ²⁺	Ni ²⁺	Co ²⁺	Ni ²⁺	Co ²⁺	Ni ²⁺
C-neat	32.5	35.0	26	28	41.3	38.8	33	31
C-I	48.8	47.5	39	38	52.5	51.3	42	41
C-II	86.3	82.5	69	66	93.8	96.3	75	77
C-III	78.8	77.5	63	62	103.8	105.0	83	84

Due to the great performance in metal ions removal, the C-III membrane was subjected to second cycle of filtration process to further study its antifouling property. As shown in Fig. 7, all cleaned-membranes for C-III showed sudden rise in flux between 180 and 210 min, attributing to the successfully removal of metal ions by deionized water during washing process prior to second filtration. However, the permeability fluxes in second filtration (210–360 min) were reducing for both pure water and metal ion solutions when comparing to first filtration (30–180 min). This is owing to the blockage of pore channels by the remained metal clusters in the membrane [61,62]. During adsorption, the sulfate function groups (SO₃⁻) on nanocellulose acted as reducing agent to synthesize Co and Ni elements from Co²⁺ and Ni²⁺ ions, which eventually aggregated to form metal microparticles [2]. This was confirmed from FESEM images presented in Fig. 8 where Co (Fig. 8a) and Ni (Fig. 8b) metal microparticles can be seen on the C-III membrane surface after adsorption process. However, the anti-fouling capability was considerably high with FR_w of 98% and 96%, while FR_p was 85% and 84% for the cleaned-Co and cleaned-Ni membranes, respectively (Fig. 8). Interestingly, the membrane could still adsorb metal ions capacities in the second filtration cycle with values of 26.4 mg/g for Co²⁺ and 27.2 mg/g for Ni²⁺ ions. Therefore, these results provide further evidence confirming the great adsorption performance of C-III membrane signifying its strong potential for removal of heavy metal ions from wastewater treatment (Fig. 9).

3.5. Statistical analysis

The reproducibility of this work was studied with replicates data. From morphology, the BET replicates data showed a prominent difference in the porosity and average pore size for each sample. Also, the insignificant standard deviation values implied the ease of reproducing the membranes with similar porous structures (Table 2). In addition, the obtained tensile test replicates data presented the tensile strength and elongations at break were significantly varying (at 95% confidence level) to each membrane sample. It was mainly affected by the complex lamination adhesion between PLA and PBS polymeric layers. Furthermore, it was noticed the less significant difference of Young's modulus in between C-neat and C-I, while also in between C-II and C-III

**Fig. 7.** Flux changes for C-III membrane in two filtration cycles.**Fig. 8.** FESEM images of C-III membrane with (a) Co and (b) Ni metal microparticles.**Fig. 9.** Reversible fouling (R_r), irreversible fouling (R_{ir}), total fouling ratio (R_t), pure water flux recovery (FR_w) and metal ion solution flux recovery (FR_p) for C-III membrane.

membranes (Table 5). This indicated the nanocellulose loadings between 1 and 2 wt% are crucial for the interaction between nanocellulose and polymers. Additionally, the standard deviation values were less than 0.1 for water contact angles (Table 6), suggesting the presence of a good interaction between membrane surface with polar groups allowing water penetration and metal ions adsorption process.

4. Conclusion

Present work findings revealed four types of CNWs filled PLA/PBS dual-layer membranes with different loadings were successfully prepared using a combined integrated water vapor-induced and crystallization-induced phase inversions method. This new fabrication method imparted a synergistic effect to the precipitation process for both polymer layers, while ultimately boosted the membrane filtration performance towards separation of heavy metal ions. The best performing membrane *i.e.*, C-III membrane showed tightly adhered polymeric layers, whilst still maintaining the high level of porosity and small pore size features. The C-I membrane exhibited the greatest heat resistance amongst all membranes, owing its low sulphated nanocellulose content. Besides this, the tensile properties were enhanced for C-II and C-III membranes attributing to the great interaction between the two polymer

layers providing a good stress transferring property within the membranes' structures. The performance of wastewater filtration showed that C-III is a reliable membrane product in removing metal ions such as Co^{2+} and Ni^{2+} by associating with its balance of great water flux, high adsorption capacity, and anti-fouling properties. Thus, it can be concluded that the newly adopted technique is a promising approach for sustainable preparation of nanocellulose-reinforced dual-layer membranes. The membranes product integrated with superior filtration performance have strong potential for application in removing heavy metal ions from wastewater streams.

Acknowledgements

The authors are grateful to Malaysian Industry-Government Group for High Technology (MIGHT) for financial support of this work Under Newton-Ungku Omar Fund Grant No: 6300873. This work is funded by Researchers Supporting Project number (RSP-2021/117), King Saud University, Riyadh, Saudi Arabia.

CRediT authorship contribution statement

Dr. Lau Kia Kian (First Author)	Collect primary data and do Experimental analysis. Design the Experiment, Interpret Characterization of obtained results and Format and finalize over all manuscript.
Dr. Mohammad Jawaid (Corresponding author)	Supervision, formal analysis, Arranged Resources, and validation. Funding acquisition, Project Administration and Validation of Data and Finalize manuscript
Prof Dr. Mohamed Mahmoud Nasef	Editing of manuscript, and Checked Final draft.
Prof Dr. H. Fouad	Funding acquisition, Resources and Editing manuscript
Dr.Zoheb Karim	Contribute in Draft, check Final draft

References

- Q.C. Xia, M.L. Liu, X.L. Cao, Y. Wang, W. Xing, S.P. Sun, Structure design and applications of dual-layer polymeric membranes, *J. Membr. Sci.* 562 (2018) 85–111, <https://doi.org/10.1016/j.memsci.2018.05.033>.
- Z. Karim, S. Claudpierre, M. Grahn, K. Oksman, A.P. Mathew, Nanocellulose based functional membranes for water cleaning: tailoring of mechanical properties, porosity and metal ion capture, *J. Membr. Sci.* 514 (2016) 418–428, <https://doi.org/10.1016/j.memsci.2016.05.018>.
- S. Bolisetty, M. Peydayesh, R. Mezzenga, Sustainable technologies for water purification from heavy metals: review and analysis, *Chem. Soc. Rev.* 48 (2019) 463–487, <https://doi.org/10.1039/C9CS00493E>.
- F. Galiano, K. Briceño, T. Marino, A. Molino, K.V. Christensen, A. Figoli, Advances in biopolymer-based membrane preparation and applications, *J. Membr. Sci.* 564 (2018) 562–586, <https://doi.org/10.1016/j.memsci.2018.07.059>.
- H. Minbu, A. Ochiai, T. Kawase, M. Taniguchi, D.R. Lloyd, T. Tanaka, Preparation of poly(L-lactic acid) microfiltration membranes by a nonsolvent-induced phase separation method with the aid of surfactants, *J. Membr. Sci.* 479 (2015) 85–94, <https://doi.org/10.1016/j.memsci.2015.01.021>.
- T. Tanaka, T. Nishimoto, K. Tsukamoto, M. Yoshida, T. Kouya, M. Taniguchi, D. R. Lloyd, Formation of depth filter microfiltration membranes of poly(L-lactic acid) via phase separation, *J. Membr. Sci.* 396 (2012) 101–109, <https://doi.org/10.1016/j.memsci.2012.01.002>.
- V. Pillay, C. Dott, Y.E. Choonara, C. Tyagi, L. Tomar, P. Kumar, L.C. du Toit, V.M. K. Ndesendo, A review of the effect of processing variables on the fabrication of electrospun nanofibers for drug delivery applications, *J. Nanomat.* (2013) 1–22, <https://doi.org/10.1155/2013/789289>.
- Y. Cai, J. Guo, C. Chen, C. Yao, S.M. Chung, J. Yao, I.S. Lee, X. Kong, Silk fibroin membrane used for guided bone tissue regeneration, *Mater. Sci. Eng. C* 70 (1) (2017) 148–154.
- O. Gokce, M. Kasap, G. Akpinar, G. Ozkoc, Preparation, characterization, and in vitro evaluation of chicken feather fiber-thermoplastic polyurethane composites, *J. Appl. Polym. Sci.* 134 (45) (2017) 1–9, <https://doi.org/10.1002/app.45338>.
- S.Z.H. Kiadeh, A. Ghaee, A. Mashak, J. Mohammadnejad, Preparation of chitosan-silica/PCL composite membrane as wound dressing with enhanced cell attachment, *Polym. Adv. Technol.* 28 (11) (2017) 1396–1408, <https://doi.org/10.1002/pat.4016>.
- A. Perazzo, V. Preziosi, S. Guido, Phase inversion emulsification: current understanding and applications, *Adv. Colloid Interface Sci.* 222 (2015) 581–599, <https://doi.org/10.1016/j.cis.2015.01.001>.
- Y. Zhao, M. Li, Z. Yuan, X. Li, H. Zhang, I.F.J. Vankelecom, Advanced charged sponge-like membrane with ultrahigh stability and selectivity for vanadium flow batteries, *Adv. Funct. Mater.* 26 (2) (2016) 210–218, <https://doi.org/10.1002/adfm.201503390>.
- K. Hamad, M. Kaseem, M. Ayyoob, J. Joo, F. Deri, Poly(lactic acid) blends: the future of green, light and tough, *Prog. Polym. Sci.* 85 (2018) 83–127, <https://doi.org/10.1016/j.progpolymsci.2018.07.001>.
- A.C. Chinyerenwa, H. Wang, Q. Zhang, Y. Zhuang, K.H. Munna, C. Ying, H. Yang, W. Xu, Structure and thermal properties of porous poly(lactic acid) membranes prepared via phase inversion induced by hot water droplets, *Polymers* 141 (2018) 62–69, <https://doi.org/10.1016/j.polymer.2018.03.011>.
- A. Gao, F. Liu, H. Shi, L. Xue, Controllable transition from finger-like pores to interconnected pores of PLLA membranes, *J. Membrane Sci.* 478 (2015) 96–104, <https://doi.org/10.1016/j.memsci.2015.01.004>.
- T. Phaechamud, S. Chitrattha, Pore formation mechanism of porous poly(DL-lactic acid) matrix membrane, *Mater. Sci. Eng. C* 61 (2016) 744–752, <https://doi.org/10.1016/j.msec.2016.01.014>.
- H. Bai, Y. Zhou, L. Zhang, Morphology and mechanical properties of a new nanocrystalline cellulose/polysulfone composite membrane, *Adv. Polym. Technol.* 34 (1) (2015), <https://doi.org/10.1002/adv.21471>.
- L. Zhong, Z. Ding, B. Li, L. Zhang, Preparation and characterization of polysulfone/sulfonated polysulfone/cellulose nanofibers ternary blend membranes, *Bioresources* 10 (2) (2012) 2936–2948, <https://doi.org/10.15376/biores.10.2.2936-2948>.
- M. Fathizadeh, A. Aroujalian, A. Raisi, Effect of added NaX nano-zeolite into polyamide as a top thin layer of membrane on water flux and salt rejection in a reverse osmosis process, *J. Membrane Sci.* 375 (2011) 88–95, <https://doi.org/10.1016/j.memsci.2011.03.017>.
- H. Huang, X. Qu, H. Dong, L. Zhang, H. Chen, Role of NaA zeolites in the interfacial polymerization process towards a polyamide nanocomposite reverse osmosis membrane, *RSC Adv.* 3 (2013) 8203–8207, <https://doi.org/10.1039/C3RA40960K>.
- N.E. Badawi, A.R. Ramadan, A.M.K. Esawi, M.E. Morsi, Novel carbon nanotube-cellulose acetate nanocomposite membranes for water filtration applications, *Desalination* 344 (2014) 79–85, <https://doi.org/10.1016/j.desal.2014.03.005>.
- H. Choi, S.H. Yoon, M. Son, E. Celik, H. Park, H. Choi, Efficacy of synthesis conditions on functionalized carbon nanotube blended cellulose acetate membrane for desalination, *Desalin. Water Treat.* 57 (2015) 7545–7554.
- D. Li, Y. Yan, H. Wang, Recent advances in polymer and polymer composite membranes for reverse and forward osmosis processes, *Prog. Polym. Sci.* 61 (2016) 104–155, <https://doi.org/10.1016/j.progpolymsci.2016.03.003>.
- O.Y. Alothman, L.K. Kian, N. Saba, M. Jawaid, R. Khiari, Cellulose nanocrystal extracted from date palm fibre: morphological, structural and thermal properties, *Ind. Crop. Prod.* 159 (2021), 113075, <https://doi.org/10.1016/j.indcrop.2020.113075>.
- A. Hachaichi, B. Kouini, L.K. Kian, M. Asim, H. Fouad, M. Jawaid, M. Sain, Nanocrystalline cellulose from microcrystalline cellulose of date palm fibers as a promising candidate for bio-nanocomposites: isolation and characterization, *Materials* 14 (2021) 5313, <https://doi.org/10.3390/ma14185313>.
- M. Rasheed, M. Jawaid, B. Parveen, A. Zuriyati, A. Khan, Morphological, chemical and thermal analysis of cellulose nanocrystals extracted from bamboo fibre, *Int. J. Biol. Macromol.* 160 (2020) 183–191, <https://doi.org/10.1016/j.ijbiomac.2020.05.170>.
- R. Arjmandi, A. Hassan, M.K.M. Haafiz, Z. Zakaria, M.S. Islam, Effect of hydrolysed cellulose nanowhiskers on properties of montmorillonite/poly(lactic acid) nanocomposites, *Int. J. Biol. Macromol.* 82 (2016) 998–1010, <https://doi.org/10.1016/j.ijbiomac.2015.11.028>.
- S.H. Sung, Y. Chang, J. Han, Development of poly(lactic acid) nanocomposite films reinforced with cellulose nanocrystals derived from coffee silverskin, *Carbohydr. Polym.* 169 (2017) 495–503, <https://doi.org/10.1016/j.carbpol.2017.04.037>.
- H. Kargarzadeh, M. Mariano, J. Huang, N. Lin, I. Ahmad, A. Dufresne, S. Thomas, Recent developments on nanocellulose reinforced polymer nanocomposites: a review, *Polymer* 132 (2017) 368–393, <https://doi.org/10.1016/j.polymer.2017.09.043>.
- S. Noorani, J. Simonsen, S. Atre, Nano-enabled microtechnology: polysulfone nanocomposites incorporating cellulose nanocrystals, *Cellulose* 14 (2007) 577–584, <https://doi.org/10.1007/s10570-007-9119-y>.
- Y. Li, T.S. Chung, Z. Huang, S. Kulprathipanja, Dual-layer polyethersulfone (PES)/BTDA-TDI/MDI co-polyimide (P84) hollow fiber membranes with a submicron PES-zeolite beta mixed matrix dense-selective layer for gas separation, *J. Membr. Sci.* 277 (2006) 28–37, <https://doi.org/10.1016/j.memsci.2005.10.008>.
- S. Bonyadi, T.S. Chung, Flux enhancement in membrane distillation by fabrication of dual layer hydrophilic-hydrophobic hollow fiber membranes, *J. Membr. Sci.* 306 (2007) 134–146, <https://doi.org/10.1016/j.memsci.2007.08.034>.
- J. Zuo, T.S. Chung, G.S. O'Brien, W. Kosar, Hydrophobic/hydrophilic PVDF/Ultem (R) dual-layer hollow fiber membranes with enhanced mechanical properties for vacuum membrane distillation, *J. Membr. Sci.* 523 (2017) 103–110, <https://doi.org/10.1016/j.memsci.2016.09.030>.
- T.Y. Liu, C.K. Li, B. Pang, B.V.D. Bruggen, X.L. Wang, Fabrication of a dual layer (CA/PVDF) hollow fiber membrane for RO concentrate treatment, *Desalination* 365 (2015) 57–69, <https://doi.org/10.1016/j.desal.2015.02.020>.
- S.T. Kao, M.Y. Teng, C.L. Li, C.Y. Kuo, C.Y. Hsieh, H.A. Tsai, D.M. Wang, K.R. Lee, J.Y. Lai, Fabricating PC/PAN composite membranes by vapor-induced phase separation, *Desalination* 233 (2008) 96–103, <https://doi.org/10.1016/j.desal.2007.09.031Get>.

- [36] L.K. Kian, M. Jawaid, H. Ariffin, Z. Karim, M.T.H. Sultan, Morphological, physico-chemical, and thermal properties of cellulose nanowhiskers from roselle fibers, *Cellulose* 26 (2019) 6599–6613, <https://doi.org/10.1007/s10570-019-02543-5>.
- [37] A. Huang, X. Peng, L. Geng, L. Zhang, K. Huang, B. Chen, Z. Gu, T. Kuang, Electrospun poly (butylene succinate)/cellulose nanocrystals bionanocomposite scaffolds for tissue engineering: preparation, characterization and in vitro evaluation, *Polym. Test.* 71 (2018) 101–109, <https://doi.org/10.1016/j.polymertesting.2018.08.027>.
- [38] A.H. Bahremand, S.M. Mousavi, A. Ahmadvand, M. Taherian, Biodegradable blend membranes of poly (butylenesuccinate)/cellulose acetate/dextran: preparation, characterization and performance, *Carbohydr. Polym.* 173 (2017) 497–507, <https://doi.org/10.1016/j.carbpol.2017.06.010>.
- [39] X. Zhang, X. Wang, Polybutylene succinate/cellulose nanocrystals: role of phthalic anhydride in squeeze oriented bionanocomposites, *Carbohydr. Polym.* 196 (2018) 254–261, <https://doi.org/10.1016/j.carbpol.2018.04.124>.
- [40] P. Daraei, N. Ghaemi, H.S. Ghari, M. Norouzi, Mitigation of fouling of polyethersulfone membranes using an aqueous suspension of cellulose nanocrystals as a nonsolvent, *Cellulose* 23 (2016) 2025–2037, <https://doi.org/10.1007/s10570-016-0937-7>.
- [41] Z. Xiong, Y. Zhong, H. Lin, F. Liu, T. Li, J. Li, PDLA/PLLA ultrafiltration membrane with excellent permeability, rejection and fouling resistance via stereocomplexation, *J. Membr. Sci.* 533 (2017) 103–111, <https://doi.org/10.1016/j.memsci.2017.03.028>.
- [42] N. Lin, Y. Chen, F. Hu, J. Huang, Mechanical reinforcement of cellulose nanocrystals on biodegradable microcellular foams with melt-compounding process, *Cellulose* 22 (2015) 2629–2639, <https://doi.org/10.1007/s10570-015-0684-1>.
- [43] L. Wang, M. Ando, M. Kubota, S. Ishihara, Y. Hikima, M. Ohshima, T. Sekiguchi, A. Sato, H. Yano, Effects of hydrophobic-modified cellulose nanofibers (CNFs) on cell morphology and mechanical properties of high void fraction polypropylene nanocomposite foams, *Compos. Part A* 98 (2017) 166–173, <https://doi.org/10.1016/j.compositesa.2017.03.028>.
- [44] H.Y. Mi, X. Jing, J. Peng, M.R. Salick, X.F. Peng, L.S. Turng, Poly(ϵ -caprolactone) (PCL)/cellulose nano-crystal (CNC) nanocomposites and foams, *Cellulose* 21 (2014) 2727–2741, <https://doi.org/10.1007/s10570-014-0327-y>.
- [45] Y. Li, S. Huang, S. Zhou, A.G. Fane, Y. Zhang, S. Zhao, Enhancing water permeability and fouling resistance of polyvinylidene fluoride membranes with carboxylated nanodiamonds, *J. Membr. Sci.* 556 (2018) 154–163, <https://doi.org/10.1016/j.memsci.2018.04.004>.
- [46] F. Luzi, E. Fortunati, A. Jiménez, D. Puglia, D. Pezzolla, G. Gigliotti, J.M. Kenny, A. Chiralt, L. Torre, Production and characterization of PLA PBS biodegradable blends reinforced with cellulose nanocrystals extracted from hemp fibres, *Ind. Crop. Prod.* 93 (2016) 276–289, <https://doi.org/10.1016/j.indcrop.2016.01.045>.
- [47] S.S. Borkotoky, P. Dhar, V. Katiyar, Biodegradable poly (lactic acid)/cellulose nanocrystals (CNCs) composite microcellular foam: effect of nanofillers on foam cellular morphology, thermal and wettability behavior, *Int. J. Biol. Macromol.* 106 (2018) 433–446, <https://doi.org/10.1016/j.ijbiomac.2017.08.036>.
- [48] K.M.Z. Hossain, R.M. Felfel, C.D. Rudd, W. Thielemans, I. Ahmed, The effect of cellulose nanowhiskers on the flexural properties of self-reinforced polylactic acid composites, *React. Funct. Polym.* 85 (2014) 193–200, <https://doi.org/10.1016/j.reactfunctpolym.2014.09.012>.
- [49] M. Planellas, M. Sacristán, L. Rey, C. Olmo, J. Aymamí, M.T. Casas, L.J. Valle, L. Franco, J. Puiggali, Micro-molding with ultrasonic vibration energy: new method to disperse nanoclays in polymer matrices, *Ultrason. Sonochem.* 21 (2014) 1557–1569, <https://doi.org/10.1016/j.ultsonch.2013.12.027>.
- [50] N. Stoyanova, D. Paneva, R. Mincheva, A. Toncheva, N. Manolova, P. Dubois, I. Rashkov, Poly(L-lactide) and poly(butylene succinate) immiscible blends: from electrospinning to biologically active materials, *Mater. Sci. Eng. C* 41 (2014) 119–126, <https://doi.org/10.1016/j.msec.2014.04.043>.
- [51] S. Mizuno, T. Maeda, C. Kanemura, A. Hotta, Biodegradability, reprocessability, and mechanical properties of polybutylene succinate (PBS) photografted by hydrophilic or hydrophobic membranes, *Polym. Degrad. Stability* 117 (2015) 58–65, <https://doi.org/10.1016/j.polymdegradstab.2015.03.015>.
- [52] V. Ojijo, T. Malwela, S.S. Ray, R. Sadiku, Unique isothermal crystallization phenomenon in the ternary blends of biopolymers polylactide and poly[(butylene succinate)-co-adipate] and nano-clay, *Polymer* 53 (2012) 505–518, <https://doi.org/10.1016/j.polymer.2011.12.007>.
- [53] M.K.M. Haafiz, A. Hassan, H.P.S.A. Khalil, I. Khan, I.M. Inuwa, M.S. Islam, M. S. Hossain, M.I. Syakir, M.R.N. Fazita, Bionanocomposite based on cellulose nanowhisiker from oil palm biomass-filled poly(lactic acid), *Polym. Test.* 48 (2015) 133–139, <https://doi.org/10.1016/j.polymertesting.2015.10.003>.
- [54] N. Peng, N. Widjojo, P. Sukitpaneenit, M.M. Teoh, G.G. Lipscomb, T.S. Chung, J. Y. Lai, Evolution of polymeric hollow fibers as sustainable technologies: past, present, and future, *Prog. Polym. Sci.* 37 (2012) 1401–1424, <https://doi.org/10.1016/j.progpolymsci.2012.01.001>.
- [55] M.S. Tijink, M. Wester, J. Sun, A. Saris, L.A. Bolhuis-Versteeg, S. Saiful, J.A. Joles, Z. Borneman, M. Wessling, D.F. Stamatialis, A novel approach for blood purification: mixed-matrix membranes combining diffusion and adsorption in one step, *Acta Biomater.* 8 (2012) 2279–2287, <https://doi.org/10.1016/j.actbio.2012.03.008>.
- [56] S. Qian, K. Sheng, PLA toughened by bamboo cellulose nanowhiskers: role of silane compatibilization on the PLA bionanocomposite properties, *Compos. Sci. Technol.* 148 (2017) 59–69, <https://doi.org/10.1016/j.compscitech.2017.05.020>.
- [57] J. Ai, L. Yang, G. Liao, H. Xia, F. Xiao, Applications of graphene oxide blended poly (vinylidene fluoride) membranes for the treatment of organic matters and its membrane fouling investigation, *Appl. Surf. Sci.* 455 (2018) 502–512, <https://doi.org/10.1016/j.apsusc.2018.05.162>.
- [58] Y. Xu, Z. Li, K. Su, T. Fan, L. Cao, Mussel-inspired modification of PPS membrane to separate and remove the dyes from the wastewater, *Chem. Eng. J.* 341 (2018) 371–382, <https://doi.org/10.1016/j.cej.2018.02.048>.
- [59] T. Fan, Z. Li, B. Cheng, J. Li, Preparation, characterization of PPS micro-porous membranes and their excellent performance in vacuum membrane distillation, *J. Membr. Sci.* 556 (2018) 107–117, <https://doi.org/10.1016/j.memsci.2018.03.084>.
- [60] C. Liu, R.N. Jin, X.K. Ouyang, Y.G. Wang, Adsorption behavior of carboxylated cellulose nanocrystal–polyethyleneimine composite for removal of Cr(VI) ions, *Appl. Surf. Sci.* 408 (2017) 77–87, <https://doi.org/10.1016/j.apsusc.2017.02.265>.
- [61] Y.H. Teow, L.M. Kam, A.W. Mohammad, Synthesis of cellulose hydrogel for copper (II) ions adsorption, *J. Environ. Chem. Eng.* 6 (2018) 4588–4597, <https://doi.org/10.1016/j.jece.2018.07.010>.
- [62] P. Liu, K. Oksman, A.P. Mathew, Surface adsorption and self-assembly of Cu(II) ions on TEMPO-oxidized cellulose nanofibers in aqueous media, *J. Colloid Interface Sci.* 464 (2016) 175–182, <https://doi.org/10.1016/j.jcis.2015.11.033>.
- [63] E.A. Danso, S. Peraniemi, T. Leiviska, A. Bhatnagar, Synthesis of S-ligand tethered cellulose nanofibers for efficient removal of Pb(II) and Cd(II) ions from synthetic and industrial wastewater, *Environ. Pollut.* 242 (2018) 1988–1997, <https://doi.org/10.1016/j.envpol.2018.07.044>.
- [64] Z. Karim, S. Monti, Microscopic hybrid membranes made of cellulose based material tuned for removing metal ions from industrial effluents, *ACS Appl. Polym. Mater.* 3 (2021) 3733–3746.
- [65] Z. Karim, S. Monti, G. Barcaro, A. Svedberg, M.A. Ansari, S. Afrin, Enhanced sieving of cellulosic microfiber membranes via tuning of interlayer spacing, *Environ. Sci. Nano* 7 (2020) 2941–2952.
- [66] Z. Karim, A. Svedberg, S. Ayub, Role of functional groups in the production of self-assembled microfibrillated cellulose hybrid frameworks and influence on separation mechanism of dye from aqueous medium, *Int. J. Biol. Macromol.* 255 (2020) 1542–1552.